analyte penetration into the porous silicon is important. The energy for analyte release from the surface may be transferred from silicon to the trapped analyte through vibrational pathways or as a result of the rapid heating of porous silicon producing H_2 (ref. 26) that releases the analyte. Alternatively, as porous silicon absorbs hydrocarbons from air or while under vacuum[27,28], rapid heating/vaporization of trapped hydrocarbon contaminants or solvent molecules may augment the vaporization and ionization of the analyte embedded in the porous silicon. The observation of DIOS-MS background ions ($m/z < 100$) at high laser intensities, consistent with aliphatic hydrocarbons, indicates that they may play a role in desorption/ionization.

The potential application of DIOS-MS is broad. The surface activity could be changed through derivatization with receptors[29], aiding the identification of ligands. In addition, the enhanced signal obtained from the ethyl phenyl surface suggests that significant improvements can be made to DIOS-MS through further investigation of surface modifications. Most existing MALDI mass spectrometers could be used to perform DIOS simply by making modifications to the MALDI sample plate (Fig. 1). Moreover, porous silicon material is inexpensive and its production simple. Porous silicon can be readily integrated with existing silicon-based technology[15], allowing, for example, its application into miniaturized chip, microfluidic chemical reactors that are lithographically etched into crystalline silicon wafers. For instance, porous silicon features as small as 20 μm and 100 nm can be produced through standard optical techniques[21] and ion implantation[30], respectively. In short, as a new desorption/ionization approach, DIOS-MS offers sensitivity, high tolerance to contaminants, no matrix interference and, because the surface properties of porous silicon can easily be tailored, more control over biomolecular mass spectrometry. □

Methods

Effective porous silicon samples for DIOS could be prepared from either n- or p-type silicon according to these general procedures. For n-type: P-doped, (100) orientation, 0.65 Ω cm resistivity Si wafers were etched for 1–3 min using +71 mA cm^{-2} current density with illumination by a 300-W tungsten filament bulb in a 1:1 solution of ethanol/49% HF (aq). For p-type: B-doped, (100) orientation, 0.01 Ω cm resistivity Si wafers were etched at 37 mA cm^{-2} current density in the dark for 3 h in a 1:1 solution of ethanol/49% HF (aq).

DIOS, MALDI and laser desorption (off a gold surface) experiments were performed on a Voyager DE-STR, time-of-flight mass spectrometer (PerSeptive Biosystems) using a pulsed nitrogen laser (Laser Science) operated at 337 nm. Once formed, ions were accelerated into the time-of-flight mass analyser with a voltage of 20 kV. Porous silicon surfaces for DIOS analysis were mounted onto the MALDI probe by adhesive tape. Analytes were dissolved in a deionized H_2O or H_2O/methanol mixture at concentrations typically ranging from 0.001 to 10.0 μM. Aliquots (0.5–1.0 μl; corresponding to 0.5 femtomol to 100 picomol analyte) of solution were deposited onto the porous surfaces and allowed to dry before DIOS mass-spectrometry analysis. After multiple usage, the porous silicon surface-regeneration procedure necessitated rinsing surfaces with deionized H_2O and methanol sequentially, and finally immersing the surface overnight in a 1:2 v/v methanol/H_2O mixture. Surfaces were rinsed with deionized H_2O then with methanol and allowed to dry before applying the analyte.

Received 17 November 1998; accepted 1 March 1999.

1. Thomson, J. J. Rays of positive electricity. *Phil. Mag.* **20,** 752–767 (1910).
2. Liu, L. K., Busch, K. L. & Cooks, R. G. Matrix-assisted secondary ion mass spectra of biological compounds. *Anal. Chem.* **53,** 109–113 (1981).
3. Barber, M., Bordoli, R. S., Sedgwick, R. D. & Tyler, A. N. Fast-atom bombardment of solids as an ion source in mass spectroscopy. *Nature* **293,** 270–275 (1981).
4. Karas, M. & Hillenkamp, F. Laser desorption ionization of proteins with molecular mass exceeding 10,000 daltons *Anal. Chem.* **60,** 2299–2301 (1988).
5. Canham, L. T. Silicon quantum wire array fabrication by electrochemical and chemical dissolution of wafers. *Appl. Phys. Lett.* **57,** 1046–1048 (1990).
6. Zenobi, R. Laser-assisted mass spectrometry. *Chimia* **51,** 801–803 (1997).
7. Zhan, Q., Wright, S. J. & Zenobi, R. Laser desorption substrate effects. *J. Am. Soc. Mass Spectr.* **8,** 525–531 (1997).
8. Hrubowchak, D. M., Ervin, M. H., Wood, M. C. & Winograd, N. Detection of biomolecules on surfaces using ion-beam-induced desorption and multiphoton resonance ionization. *Anal. Chem.* **63,** 1947–1953 (1991).
9. Varakin, V. N., Lunchev, V. A. & Simonov, A. P. Ultraviolet-laser chemistry of adsorbed dimethyl-cadmium molecules. *High En. Chem.* **28,** 406–411 (1994).
10. Wang, S. L., Ledingham, K. W. D., Jia, W. J. & Singhal, R. P. Studies of silicon nitride (Si_3N_4) using laser ablation mass spectrometry. *Appl. Surf. Sci.* **93,** 205–210 (1996).
11. Posthumus, M. A., Kistemaker, P. G., Meuzelaar, H. L. C. & Ten Noever de Brauw, M. C. Laser desorption–mass spectrometry of polar nonvolatile bio-organic molecules. *Anal. Chem.* **50,** 985–991 (1978).
12. Macfarlane, R. D. & Torgerson, D. F. Californium-252 plasma desorption mass spectroscopy. *Science* **191,** 920–925 (1976).
13. Siuzdak, G. in *Mass Spectrometry for Biotechnology* 162 (Academic, San Diego, 1996).
14. Buriak, J. M. & Allen, M. J. Lewis acid mediated functionalization of porous silicon with substituted alkenes and alkynes. *J. Am. Chem. Soc.* **120,** 1339–1340 (1998).
15. Cullis, A. G., Canham, L. T. & Calcott, P. D. J. The structural and luminescence properties of porous silicon. *J. Appl. Phys.* **82,** 909–965 (1997).
16. Hillenkamp, F., Karas, M., Beavis, R. C. & Chait, B. T. Matrix-assisted laser desorption ionization mass spectrometry of biopolymers. *Anal. Chem.* **63,** A1193–A1202 (1991).
17. Benninghoven, A., Rüdenauer, F. G. & Werner, H. W. (eds) *Secondary Ion Mass Spectrometry* 1227 (Wiley, New York, 1987).
18. Amato, G. & Rosenbauer, M. in *Optoelectronic Properties of Semiconductors and Superlattices* (eds Amato, G., Delerue, C. & Bardeleben, H.-J.v.) 3–52 (Gordon and Breach, Amsterdam, 1997).
19. Sailor, M. J. & Lee, E. J. Surface chemistry of luminescent silicon nanocrystallites. *Adv. Mater.* **9,** 783–793 (1997).
20. Stewart, M. P. & Buriak, J. M. Photopatterned hydrosilylation on porous silicon. *Angew. Chem. Int. Edn* **37,** 3257–3261 (1998).
21. Doan, V. V. & Sailor, M. J. Photolithographic fabrication of micron-dimension porous Si structures exhibiting visible luminescence. *Appl. Phys. Lett.* **60,** 619–620 (1992).
22. Lidgard, R. & Duncan, M. W. Utility of matrix-assisted laser desorption ionization time-of-flight mass spectrometry for the analysis of low molecular weight compounds. *Rapid Commun. Mass Spectr.* **9,** 128–132 (1995).
23. Knochenmuss, R., Dubois, F., Dale, M. J. & Zenobi, R. The matrix suppression effect and ionization mechanisms in matrix-assisted laser desorption/ionization. *Rapid Commun. Mass Spectr.* **10,** 871–877 (1996).
24. Canham, L. T. in *Properties of Porous Silicon* (ed. Canham, L. T.) 83–88 (Institution of Electrical Engineers, London, 1997).
25. Hérino, R. in *Properties of Porous Silicon* (ed. Canham, L. T.) 89–96 (Institution of Electrical Engineers, London, 1997).
26. Ogata, Y. H., Kato, F., Tsuboi, T. & Sakka, T. J. Changes in the environment of hydrogen in porous silicon with thermal annealing. *Electrochem. Soc.* **145,** 2439–2444 (1998).
27. Canham, L. T. in *Properties of Porous Silicon* (ed. Canham, L. T.) 154–157 (Institution of Electrical Engineers, London, 1997).
28. Canham, L. T. in *Properties of Porous Silicon* (ed. Canham, L. T.) 44–50 (Institution of Electrical Engineers, London, 1997).
29. O'Donnell, M. J., Tang, K., Koster, H. & Smith, C. L. High density, covalent attachment of DNA to silicon wafers for analysis by MALDI-TOF mass spectrometry. *Anal. Chem.* **69,** 2438–2443 (1997).
30. Schmuki, P., Erickson, L. E. & Lockwood, D. J. Light emitting micropatterns of porous Si created at surface defects. *Phys. Rev. Lett.* **80,** 4060–4063 (1998).

Acknowledgements. We thank J. Boydston, Z. Shen, R. G. Cooks and M. Duncan for their comments, T. Hollenbeck for suggesting the acronym DIOS, K. Harris for his initial analyses of porous silicon surfaces, and M. P. Stewart and T. Geders for preparing oxidized and p-type porous silicon samples. G.S. is grateful for partial funding by an NIH grant; J.M.B. thanks Purdue University for support and the Camille and Henry Dreyfus Foundation for a New Faculty Award.

Correspondence and requests for materials should be addressed to J.M.B. and G.S. (e-mail: buriak@purdue.edu and siuzdak@scripps.edu).

Growing range of correlated motion in a polymer melt on cooling towards the glass transition

Christoph Bennemann*‡, Claudio Donati*†, Jörg Baschnagel‡ & Sharon C. Glotzer*

** Center for Theoretical and Computational Materials Science, and Polymers Division, National Institute of Standards and Technology, Gaithersburg, Maryland 20899, USA*

† Dipartimento di Fisica e Istituto Nazionale per la Fisica della Materia, Universita' di Roma 'La Sapienza', Piazzale Aldo Moro 2, I-00185 Roma, Italy

‡ Institut für Physik, Johannes Gutenberg Universität, Staudinger Weg 7, 55099 Mainz, Germany

Many liquids cooled to low temperatures form glasses (amorphous solids) instead of crystals. As the glass transition is approached, molecules become localized and relaxation times increase by many orders of magnitude[1]. Many features of this 'slowing down' are reasonably well described[2] by the mode-coupling theory of supercooled liquids[3]. The ideal form of this theory predicts a dynamical critical temperature T_c at which the

molecules become permanently trapped in the 'cage' formed by their neighbours, and vitrification occurs. Although there is no sharp transition, because molecules do eventually escape their cage, its signature can still be observed in real and simulated liquids. Unlike conventional critical phenomena (such as the behaviour at the liquid–gas critical point), the mode-coupling transition is not accompanied by a diverging static correlation length. But simulation[4–10] and experiment[11,12] show that liquids are dynamically heterogeneous, suggesting the possibility of a relevant 'dynamical' length scale characterizing the glass transition. Here we use computer simulations to investigate a melt of short, unentangled polymer chains over a range of temperatures for which the mode-coupling theory remains valid. We find that although density fluctuations remain short-ranged, spatial correlations between monomer displacements become long-ranged as T_c is approached on cooling. In this way, we identify a growing dynamical correlation length, and a corresponding order parameter, associated with the glass transition. This finding suggests a possible connection between well established concepts in critical phenomena and the dynamics of glass-forming liquids.

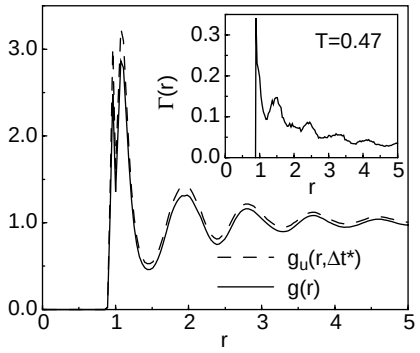

Figure 1 Displacement–displacement correlation function $g_u(r, \Delta t)$ and pair correlation function $g(r)$ plotted versus r at $T = 0.47$ and $\Delta t = 277.76$. Inset: $\Gamma(r) \equiv [g_u(r, \Delta t)/g(r)] - 1$, plotted versus r. Note that if the displacement of monomers were spatially uncorrelated then $g_u(r, \Delta t)$ and $g(r)$ would be identical for all r. Hence, it is deviations of $g_u(r, \Delta t)$ from $g(r)$ that demonstrate spatial displacement correlations in excess of those expected from $g(r)$ alone. Results were obtained by a molecular dynamics simulation of a polymer melt consisting of about 120 chains of 10 monomers each. Monomers interact via a Lennard-Jones potential, and nearest-neighbour monomers along a chain are connected by a FENE anharmonic spring potential[19–21]. Length and temperature scales are measured in Lennard-Jones units. Simulations are carried out at constant pressure ($P = 1$) and in a temperature range (T) from 0.70–0.46, corresponding to densities of $0.91 \lesssim n \lesssim 1.04$. Each state point is fully equilibrated before all measurements. For each state point, all quantities are averaged over 150–200 independent time origins. This melt is well described by ideal mode-coupling theory with $T_c = 0.450 \pm 0.005$ and $n_c = 1.042 \pm 0.010$ (refs 19–21).

We consider a polymer melt consisting of chains of M identical monomers. Let the position of each monomer i at a time t be denoted $\mathbf{r}_i(t)$. As a measure of the local motion, we introduce the scalar displacement $\mu_i(t, \Delta t) = |\mathbf{r}_i(t + \Delta t) - \mathbf{r}_i(t)|$ over some interval of time Δt, starting from a reference time t. We examine the spatial correlations of these displacements by modifying the definition of the usual static density–density correlation function $G(\mathbf{r})$ (ref. 13) so that the contribution of a monomer i to the correlation function is weighted by μ_i. That is, we define a 'displacement–displacement' correlation function[14,15],

$$G_u(\mathbf{r}, \Delta t) = \int d\mathbf{r}' \langle [u(\mathbf{r}' + \mathbf{r}, t, \Delta t) - \langle u \rangle][u(\mathbf{r}', t, \Delta t) - \langle u \rangle] \rangle$$

where

$$u(\mathbf{r}, t, \Delta t) = \sum_{i=1}^{N} \mu_i(t, \Delta t) \delta(\mathbf{r} - \mathbf{r}_i(t))$$

Here $\langle \ldots \rangle$ indicates an ensemble average, and N is the total number of monomers present in a particular configuration. $G_u(\mathbf{r}, \Delta t)$ measures the correlations of fluctuations of local displacements away from their average value $\langle u \rangle \equiv \langle u(\mathbf{r}, t, \Delta \mathbf{t}) \rangle$. As the melt is isotropic, $G(\mathbf{r})$ and $G_u(\mathbf{r}, \Delta t)$ only depend on $r = |\mathbf{r}|$. We define

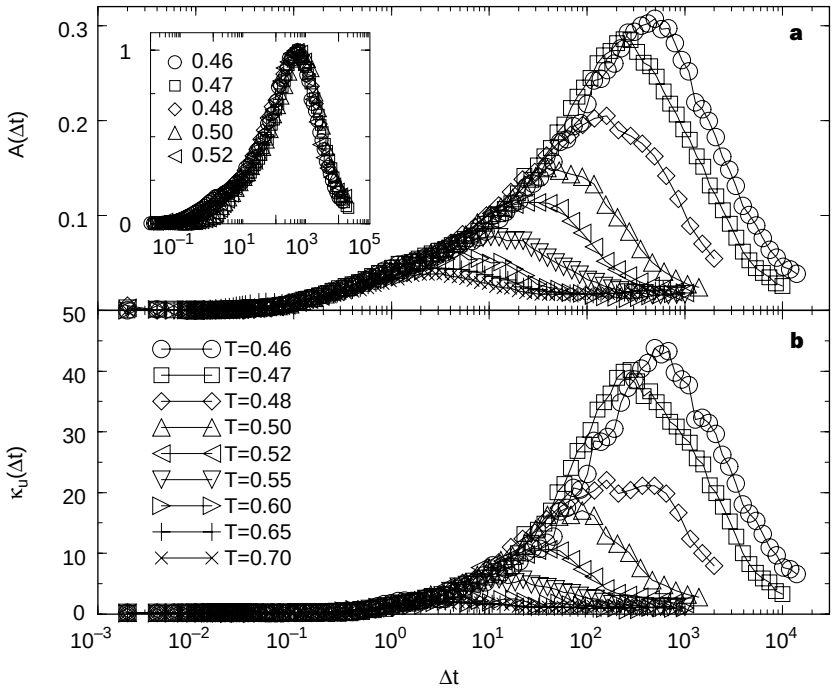

Figure 2 Time dependence of the 'excess' correlation $A(\Delta t)$ and the susceptibility $\kappa_u(\Delta t)$. **a**, $A(\Delta t)$ plotted versus Δt for different T. Inset: $A(\Delta t)/A(\Delta t^*)$ plotted versus $\Delta t/\Delta t^*$ for lowest five temperatures, showing that the data collapse onto a single master curve over several decades. **b**, $\kappa_u(\Delta t)$ plotted versus Δt for the same T as in **a**. Although not as clean, $\kappa_u(\Delta t)$ appears to show the same data collapse as that for $A(\Delta t)$ (inset).

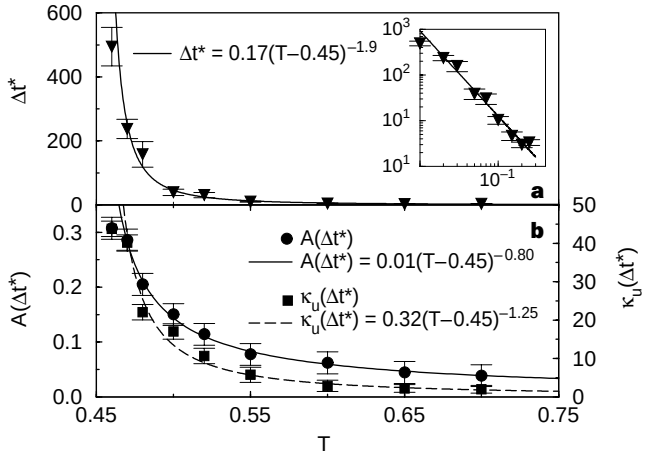

Figure 3 Temperature dependence of the 'excess' correlation $A(\Delta t)$ and the 'susceptibility' $\kappa_u(\Delta t)$. **a**, Time Δt^* when $A(\Delta t)$ is largest, plotted versus T. The solid curve is a power-law fit, $\Delta t^* \sim (T - T_c)^{-\gamma}$, with $T_c = 0.450 \pm 0.005$ and $\gamma = 1.87 \pm 0.15$. Inset: same data and fit, plotted log–log versus $T - 0.450$. **b**, κ_u and A evaluated at Δt^*, plotted versus T. The curves are power-law fits to the data obtained with $T_c = 0.450$, as indicated. Excellent fits are obtained for a small range of $T_c = 0.450 \pm 0.005$, and corresponding $\gamma = 0.80 \pm 0.07$ for A, and $\gamma = 1.25 \pm 0.11$ for κ. Note that the data point for $T = 0.46$ is excluded from all fits. All fits are made by subtracting T_c from T, taking the log of the ordinate and the abcissa, and performing a linear regression of the logged data to obtain the exponent and prefactor of the power law for that value of T_c. Error bars on the exponents are obtained by varying T_c between the lower and upper bounds quoted here.

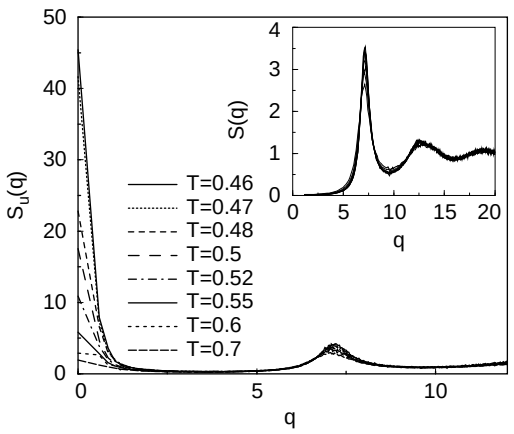

Figure 4 Displacement 'structure factor' $S_u(q, \Delta t)$ plotted versus wavevector $\mathbf{q}$ for different T, and for $\Delta t = \Delta t^*$ $S_u(\mathbf{q}, \Delta t) = \langle (N\overline{\mu^2})^{-1} \Sigma_{i=1}^{N} \Sigma_{j=1}^{N} \mu_i(t, \Delta t^*) \mu_j(t, \Delta t^*) \exp[-i\mathbf{q}(\mathbf{r}_i(t) - \mathbf{r}_j(t))] \rangle$. The values at $q = 0$ are obtained from the fluctuations in U via the relation $S_u(0, \Delta t) = \bar{\mu}^2 n T \kappa_u / \overline{\mu^2}$. Inset: static structure factor $S(q)$ for four different T, defined as $S(\mathbf{q}) = \langle N^{-1} \Sigma_{i=1}^{N} \Sigma_{j=1}^{N} \exp[-i\mathbf{q}(\mathbf{r}_i - \mathbf{r}_j)] \rangle$.

the 'total displacement' $U(t, \Delta t) = \int d\mathbf{r} u(\mathbf{r}, t, \Delta t)$ and its ensemble average $\langle U \rangle \equiv \langle U(t, \Delta t) \rangle$. In a constant-N ensemble, both $\langle u \rangle$ and $\langle U \rangle$ are readily evaluated from the mean displacement $\bar{\mu} \equiv \langle N^{-1} \Sigma_{i=1}^{N} \mu_i(t, \Delta t) \rangle$: $\langle u \rangle = \bar{\mu} n$ and $\langle U \rangle = \bar{\mu} N$, where n $(= N/V)$ is the density. In equilibrium, $\langle u \rangle$, $\langle U \rangle$, $\bar{\mu}$ and $G_u(\mathbf{r}, \Delta t)$ do not depend on t, but they retain a dependence on Δt which we address below.

$G_u(\mathbf{r}, \Delta t)$ can be written so as to identify a spatial correlation function $g_u(\mathbf{r}, \Delta t)$, analogous to the pair correlation $g(\mathbf{r})$ conventionally used to characterize the structure of a liquid

$$G_u(\mathbf{r}, \Delta t) = N\overline{\mu^2}\delta(\mathbf{r}) + \langle u \rangle \langle U \rangle [g_u(\mathbf{r}, \Delta t) - 1]$$

where

$$g_u(\mathbf{r}, \Delta t) = \frac{1}{\langle u \rangle \langle U \rangle} \left\langle \sum_{i=1}^{N} \sum_{\substack{j=1 \\ j \neq i}}^{N} \mu_i(t, \Delta t) \mu_j(t, \Delta t) \delta(\mathbf{r} + \mathbf{r}_j(t) - \mathbf{r}_i(t)) \right\rangle$$

The mean-square displacement $\overline{\mu^2} \equiv \langle \frac{1}{N} \Sigma_{i=1}^{N} \mu_i^2(t, \Delta t) \rangle$ also depends on Δt. The fluctuations of U are related to the volume integral of $G_u(\mathbf{r}, \Delta t)$:

$$\langle [U - \langle U \rangle]^2 \rangle = \int d\mathbf{r} G_u(\mathbf{r}, \Delta t) \equiv \langle U \rangle \langle u \rangle k T \kappa_u \qquad (1)$$

Here we have defined the quantity κ_u in analogy to the isothermal compressibility κ, which is proportional to the volume integral of $G(\mathbf{r})$ (ref. 16). Recall that near a conventional critical point where κ diverges, long-range behaviour is observed for $G(\mathbf{r})$ that is associated with the occurrence of macroscopic density fluctuations[16]. It is thus possible to determine the large-r behaviour of $G_u(\mathbf{r})$ from the fluctuations of U, just as the large-r behaviour of $G(\mathbf{r})$ can be determined from the fluctuations of N (ref. 16).

In the present polymer melt, as in most glass-forming liquids[17,18], we observe no growing static compressibility, and thus no long-range correlations in the monomer positions, on cooling, despite an increase of relaxation times of 3–4 orders of magnitude over the range of T investigated[19–21]. However, a growing range of correlation can be detected in the particle motion. In Fig. 1, we show $g_u(r, \Delta t)$ as a function of r for $T = 0.47$ (all quantities are reported in reduced units; see legend). This temperature is within 5% of the mode-coupling critical temperature for this system, $T_c = 0.450 \pm 0.005$ (refs 19–21). The corresponding pair correlation function $g(r)$ for $T = 0.47$ is also shown. We find that for $\Delta t = 277.76$ ($\gg$ the microscopic 'collision' time), $g_u(r, \Delta t)$ is appreciably higher than $g(r)$ for values of r up to several monomer diameters. The excess correlation of the monomer displacements beyond that of their static structure is made clearer in the inset of Fig. 1, where we show the function $\Gamma(r, \Delta t) \equiv [g_u(r, \Delta t)/g(r)] - 1$.

The extent to which monomer displacements are correlated depends strongly on the choice of Δt. Figure 2a shows the total excess correlation $A(\Delta t) \equiv \int dr \Gamma(r, \Delta t)$ as a function of Δt. We find that there is a time interval Δt^* at which A is a maximum and that both the maximum value of A and Δt^* increase with decreasing T. Hence for each T, the spatial correlation of monomer displacements is most prominent at Δt^*. As shown in the inset of Fig. 2a, all curves for $T \leq 0.55$ collapse onto a single master curve over several decades when t is scaled by Δt^* and A is scaled by $A(\Delta t^*)$, demonstrating that Δt^* is a characteristic time for this melt. We therefore evaluate all quantities henceforth using $\Delta t = \Delta t^*$. Figure 3a shows that Δt^* follows a power law with T: an excellent fit to the form $\Delta t^* \sim (T - T_c)^{-\gamma}$ is obtained when $T_c = 0.450 \pm 0.005$, and yields $\gamma = 1.87 \pm 0.15$. Despite the large error, this value for γ agrees better with the exponent governing the apparent vanishing of the self-diffusion coefficient D at T_c ($\gamma_D = 1.82 \pm 0.02$) than with that governing the divergence of the structural relaxation time τ_α ($\gamma_\tau = 2.09 \pm 0.07$; ref. 20).

As κ_u quantifies the total magnitude (integrated over space) of the displacement correlations measured by $G_u(\mathbf{r}, \Delta t)$, we expect κ_u to behave like A. We evaluate κ_u from equation (1) and confirm that κ_u exhibits (Fig. 2b) the same behaviour as A: κ_u goes to zero at short and long times, and has a maximum at a T-dependent Δt^*. In Fig. 3b, we show the T-dependence of A and κ_u at Δt^*. Both grow monotonically with decreasing T, indicating that the range of the correlation grows with decreasing T. We find that both quantities follow a power law with a singular temperature $T_c = 0.450$, demonstrating that $G_u(r, \Delta t^*)$ becomes long-ranged as T approaches the mode-coupling temperature.

To estimate a correlation length associated with these displacement correlations, we evaluated $S_u(q, \Delta t^*)$ for different T (Fig. 4). For intermediate and large q, $S_u(q, \Delta t^*)$ coincides with the static

structure factor $S(q)$. However, for $q \rightarrow 0$, a peak develops and grows with decreasing T, again demonstrating the presence of increasing long-range behaviour for $G_u(r, \Delta t^*)$. No such growing peak at $q = 0$ appears in $S(q)$ (Fig. 4, inset). By analogy with conventional critical phenomena, we have attempted to fit $S_u(q, \Delta t^*)$ by an Ornstein–Zernike form, $S_u(q) \propto 1/(1 + \xi^2 q^2)$, where ξ is the correlation length[16]. This form fits well at the highest T, but fails on approaching T_c, possibly because of finite size effects. Larger simulations may be required to determine accurately the correct functional form for S_u at small q. Nevertheless, the data show unambiguously that as $T \rightarrow T_c$, spatial correlations between the displacement of monomers become increasingly long-ranged.

Our simulations reveal a dynamical length scale relevant both to the mode-coupling dynamical transition and the glass transition. In this way we provide a bridge between the phenomenon of dynamical heterogeneity and current theories of supercooled liquids and vitrification. Remarkably, our findings are qualitatively identical to new results for simulated $Ni_{80}P_{20}$, a model metallic glassformer[14], showing that the correlated monomer motion above T_c is neither due to nor strongly affected by chain connectivity. Instead, the striking similarity between $Ni_{80}P_{20}$ and the present polymer melt suggests that correlated motion is a universal feature of (at least fragile[1]) glass-forming liquids. Furthermore, we have identified a fluctuating dynamical variable U in this polymer melt whose fluctuations become long-ranged and appear to diverge at T_c, and which thus behaves much like a static order parameter on approaching a second-order phase transition—albeit one that is not obviously accessible to traditional scattering experiments, but may be measurable in optical microscopy experiments on colloidal suspensions. Our findings suggest that substantial shifts in T_c could be observed by confining glass-forming liquids and melts, thereby limiting the divergence that can occur. Whether this could also explain the confinement-induced shifts of T_g observed experimentally[22–26] needs to be investigated. Our results indicate that it may be possible to obtain further insight into the nature of supercooled, glass-forming liquids using an extension to dynamically defined quantities of the framework of ordinary critical phenomena. □

Received 15 December 1998; accepted 2 March 1999.

1. Ediger, M. D., Angell, C. A. & Nagel, S. R. Supercooled liquids and glasses. *J. Phys. Chem.* **100,** 13200–13212 (1996).
2. Yip, S. & Nelson, P. (eds) *Transport Theory. Stat. Phys.* **24,** 755–1270 (1995).
3. Götze, W. & Sjögren, L. The mode coupling theory of structural relaxations. *Transport Theory Stat. Phys.* **24,** 801–853 (1995).
4. Hiwatari, Y. & Muranaka, T. Structural heterogeneity in supercooled liquids and glasses. *J. Non-Cryst. Solids* **235–237,** 19–26 (1998).
5. Perera, D. & Harrowell, P. A two-dimensional glass: microstructure and dynamics of a 2D binary mixture. *J. Non-Cryst. Solids* **235–237,** 314–319 (1998).
6. Onuki, A. & Yamamoto, Y. Kinetic heterogeneities and non-linear rheology of highly supercooled liquids. *J. Non-Cryst. Solids* **235–237,** 34–40 (1998).
7. Doliwa, B. & Heuer, A. Cage effect, local anisotropies, and dynamic heterogeneities at the glass transition: a computer study of hard spheres. *Phys. Rev. Lett.* **80,** 4915–4919 (1998).
8. Kob, W., Donati, C., Plimpton, S. J., Poole, P. H. & Glotzer, S. C. Dynamical heterogeneities in a supercooled Lennard-Jones liquid. *Phys. Rev. Lett.* **79,** 2827–2930 (1997).
9. Donati, C. *et al.* String-like clusters and cooperative motion in a model glass-forming liquid. *Phys. Rev. Lett.* **80,** 2338–2341 (1998).
10. Donati, C., Glotzer, S. C., Poole, P. H., Kob, W. & Plimpton, S. J. Spatial correlations of mobility and immobility in a glass-forming Lennard-Jones liquid. *Phys. Rev. E.* (submitted).
11. Böhmer, R. *et al.* Nature of the non-exponential primary relaxation in structural glass-formers probed by dynamically selective experiments. *J. Non-Cryst. Solids* **235–237,** 1–9 (1998).
12. Cicerone, M. T., Blackburn, F. & Ediger, M. D. Anomalous diffusion of probe molecules in polystyrene: evidence for spatially heterogeneous segmental dynamics. *Macromolecules* **28,** 8224–8232 (1995).
13. Hansen, J. P. & McDonald, I. R. *Theory of Simple Liquids* (Academic, London, 1986).
14. Donati, C., Glotzer, S. C. & Poole, P. H. Growing spatial correlations of particle displacements in a simulated liquid on cooling toward the glass transition. *Phys. Rev. Lett.* (in the press).
15. Glotzer, S. C., Jan, N., Lookman, T., MacIsaac, A. B. & Poole, P. H. Dynamical heterogeneity in the Ising spin glass. *Phys. Rev. E* **57,** 7350–7353 (1998).
16. Stanley, H. E. *Introduction to Phase Transitions and Critical Phenomena* (Oxford University Press, New York, 1971).
17. van Blaaderen, A. & Wiltzius, P. Real-space structure of colloidal hard-sphere glasses. *Science* **270,** 1177–1179 (1995).
18. Leheny, R. L. *et al.* Structural studies of an organic liquid through the glass transition. *J. Chem. Phys.* **105,** 7783–7794 (1996).
19. Bennemann, C., Paul, W., Binder, K. & Dünweg, B. Molecular-dynamics simulations of the thermal glass transition in polymer melts: α-relaxation behavior. *Phys. Rev. E* **57,** 843–851 (1998).
20. Bennemann, C., Baschnagel, J. & Paul, W. Molecular-dynamics simulation of a glassy polymer melt: incoherent scattering function. *Eur. Phys. J. B* (in the press).
21. Bennemann, C., Paul, W., Baschnagel, J. & Binder, K. Investigating the influence of different thermodynamic paths on the structural relaxation in a glass forming polymer melt. *J. Phys. Cond. Mat.* (in the press).
22. Jerome, B. & Commandeur, J. Dynamics of glasses below the glass transition. *Nature* **386,** 589–592 (1997).
23. Forrest, J. A., Dalnoki-Veress, K. & Dutcher, J. R. Interface and chain confinement effects on the glass transition temperature of thin polymer films. *Phys. Rev. E* **56,** 5705–5515 (1997).
24. Wallace, W. E., van Zanten, J. H. & Wu, W .L. Influence of an impenetrable interface on a polymer glass-transition temperature. *Phys. Rev. E* **52,** R3329–R3332 (1995).
25. Jackson, C. L. & McKenna, G. B. The glass transition of organic liquids confined to small pores. *J. Non-Cryst. Solids* **131–133,** 221–224 (1991).
26. Arndt, M., Stannarius, R., Groothues, H. & Kremer, F. Length scale of cooperativity in the dynamic glass transition. *Phys. Rev. Lett.* **79,** 2077–2080 (1997).

Correspondence and requests for materials should be addressed to S.C.G. (e-mail: sharon.glotzer@nist.gov).

Global changes in intensity of the Earth's magnetic field during the past 800 kyr

Yohan Guyodo*† & Jean-Pierre Valet*

Institut de Physique du Globe de Paris, UMR CNRS 7577, 4, Place Jussieu, 75262 Paris Cedex 05, France

Recent advances in palaeomagnetic and dating techniques have led to increasingly precise records of the relative intensity of the Earth's past magnetic field at numerous field sites. The compilation and analysis of these records can provide important constraints on changes in global magnetic field intensity and therefore on the Earth's geodynamo itself. A previous compilation for the past 200 kyr integrated 17 marine records into a composite curve[1], with the geomagnetic origin of the signal supported by an independent analysis of ^{10}Be production made on different cores[2]. The persistence of long-term features in the Earth's magnetic intensity or the existence of long-term periodic changes cannot, however, be resolved in this relatively short time span. Here we present the integration of 33 records of relative palaeointensity[3–19] into a composite curve spanning the past 800 kyr. We find that the intensity of the Earth's dipole field has experienced large-amplitude variations over this time period with pronounced intensity minima coinciding with known excursions in field direction, reflecting the emergence of non-dipole components. No stable periodicity was found in our composite record and therefore our data set does not support the hypothesis that the Earth's orbital parameters have a direct and strong influence on the geodynamo.

We constructed the database (Table 1) by selecting records obtained after appropriate normalization of magnetization intensity. All the studies have been published with the exception of a high-resolution sequence from core ODP-1021[18]. In addition to the data involved in the composite curve[1] referred to above ('Sint-200'), the present selection includes 16 new records relatively well distributed around the globe, 10 of which document the interval 600–800 kyr ago (Table 1). In most cases, dating was obtained by correlation to reference curves of oxygen-isotope (δ^{18}O) variations or other palaeoclimate proxies such as low field susceptibility or density. The age model defined by the δ^{18}O reference curve of Bassinot *et al.*[20] has been applied to records older than 300 kyr; the reference curve of Martinson *et al.*[21] was preferred for records younger than 300 kyr because of its higher resolution. An alternative approach was used for three cores (RC10-167, KS87-752 and P226) with no obvious correlation between the palaeoclimate proxies and the δ^{18}O reference curve. Following previous studies[1,10], these individual records of palaeointensity were correlated with a preliminary stack derived from the other well dated curves. In a second

† Present address: Department of Geology, University of Florida, Gainesville, Florida 32611, USA.